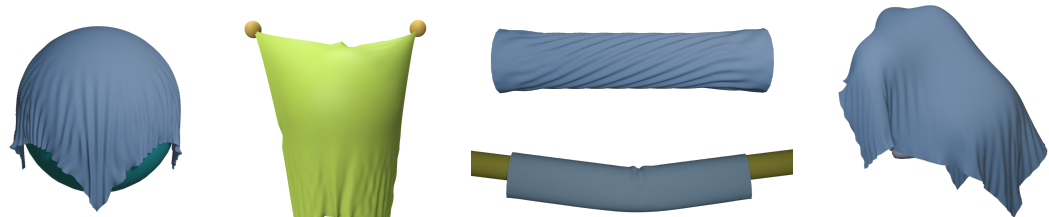


1 Dynamic Wrinkling on Coarsely-Meshed Cloth

2

3 ANONYMOUS AUTHOR(S)

4 SUBMISSION ID: 33



15 Fig. 1. Our dynamic wrinkling model that extends Chen et al. [2021]'s static framework for dynamic wrinkling
16 at interactive rates.

17 We present a technique for simulating detailed cloth dynamics on coarse meshes at interactive rates, by
18 coupling the base mesh simulation with dynamic wrinkles in a physically consistent manner. Building on the
19 wrinkle parameterization introduced by [Chen et al. 2021], we introduce a dynamics model for a cloth sheet
20 represented as a superposition of a base surface and a wrinkle distribution parameterized by spatially varying
21 amplitude and frequency. Our model incorporates two-way coupling of the base surface and the wrinkle
22 parameters, allowing the base deformation to drive emergence of wrinkles and permitting compression of
23 the base surface in turn. To deform the mesh using the computed wrinkle parameters, we also introduce a
24 simple phase reconstruction strategy that produces dynamically evolving, temporally coherent wrinkles on
25 the simulated mesh.

26 CCS Concepts: • Computing methodologies;

27 Additional Key Words and Phrases: Physics-based simulation, computer graphics

28 **ACM Reference Format:**

29 Anonymous Author(s). 2026. Dynamic Wrinkling on Coarsely-Meshed Cloth. *Proc. ACM Comput. Graph.
30 Interact. Tech.* 1, 1 (January 2026), 16 pages. <https://doi.org/10.1145/nnnnnnnn.nnnnnnnn>

32 1 Introduction

33 Cloth simulation techniques in computer graphics have seen dramatic improvements over the last
34 several decades. Offline simulations of garments with many millions of vertices can model fabric at
35 sub-millimeter scales [Wang 2021] and on the level of individual yarns [Cirio et al. 2014; Kaldor et al.
36 2008]. However, for interactive applications, simulation quality is still limited by mesh resolution,
37 and modeling clothing with realistic details such as wrinkles and folds remains a challenge.

38 The fundamental challenge in the interactive setting is that the cost of simulation rises rapidly
39 with mesh resolution. Discretizing the garment at a fine enough resolution to capture all visually
40 important details such as emergent wrinkles is infeasible to simulate at interactive rates. On the

42 Permission to make digital or hard copies of all or part of this work for personal or classroom use is granted without fee
43 provided that copies are not made or distributed for profit or commercial advantage and that copies bear this notice and the
44 full citation on the first page. Copyrights for components of this work owned by others than the author(s) must be honored.
45 Abstracting with credit is permitted. To copy otherwise, or republish, to post on servers or to redistribute to lists, requires
46 prior specific permission and/or a fee. Request permissions from permissions@acm.org.

47 © 2026 Copyright held by the owner/author(s). Publication rights licensed to ACM.

48 ACM 2577-6193/2026/1-ART

49 <https://doi.org/10.1145/nnnnnnnn.nnnnnnnn>

other hand, simulations on coarser meshes suffer not just from a lack of fine details, but also visually objectionable artifacts such as finite element locking [Koh et al. 2015]. In essence coarse discretizations smooth out the deformation energies resulting in loss of high frequency details, whereas fine meshes increase the problem stiffness requiring highly accurate solvers.

Wrinkles play an important role in providing visual plausibility for cloth simulations. Recently, Chen et al. [2021] have introduced a physics-based technique for modeling fine wrinkles on coarsely meshed sheets, by first simulating the deformation of the coarse mesh and then computing the spatially varying wrinkle parameters (amplitude and phase). Their technique yields impressive agreement with reference high-resolution simulations in many cases, but only works for static drapes and does not support animation. Their follow-up work [Chen et al. 2023a] allows animating wrinkles evolving over time through a spacetime optimization, which is not suitable for interactive applications.

In this work, we build on the wrinkle representation of Chen et al. [2021] to provide a physically consistent method for dynamic cloth simulation with fine wrinkles on coarse cloth meshes. Our approach supports two-way coupling of the wrinkle parameters with the coarse base mesh, allowing the emerging wrinkles to affect the mechanical behaviour of the base mesh and reducing locking artifacts. We also provide a fast method to synthesize animated wrinkles in a temporally coherent manner.

Our main contributions are:

- (1) We present the first physics-based model for the dynamics of an elastic sheet represented as a mid-surface coupled with wrinkle amplitudes and frequencies.
- (2) We design a simple spatial discretization and time stepping scheme for simulation of such wrinkle-augmented sheets, suitable for fast iterative methods such as vertex block descent.
- (3) We present a fast method for temporally coherent reconstruction of phases from the frequency wrinkle field. Crucially, our approach handles the sign ambiguity in the frequency field that is not supported by existing methods.

2 Related work

Many cloth simulation techniques have appeared in graphics literature, from mass-spring models [Breen 1993; Choi and Ko 2002; Provot 2001] to finite elements Narain et al. [2012]; Thomaszewski et al. [2006] and yarn-level simulation [Cirio et al. 2014; Kaldor et al. 2008].

In this work, we focus on mesh-based cloth simulation techniques suitable for real-time simulation. At lower mesh resolutions, such simulations suffer from severe artifacts such as element locking [English and Bridson 2008; Jin et al. 2017]. These problems can be mitigated by refining the mesh to provide enough degrees of freedom for wrinkles to appear [Narain et al. 2012; Zhang et al. 2025], but this increases the cost of the simulation and is not feasible in interactive applications. Alternatively, locking can also be reduced by lowering the stiffness of the cloth, which leads to an objectionably stretchy appearance [Goldenthal et al. 2007].

A promising approach to overcoming these challenges is to conceptually separate the fine-scale details such as wrinkles and folds from the overall low-frequency “base” deformation of the sheet, allowing a coarse simulation mesh to be responsible only for the latter, and then augment the simulation with wrinkle details as a postprocess. The seminal work of Rohmer et al. [2010] traced wrinkle curves along the simulated sheet using the stretch tensor and used them to deform the surface. Building on this approach, Gillette et al. [2015] described a careful stretch tensor estimation process to add wrinkles to extremely low-poly cloth animation with no reference shape. Other works designing procedural models for wrinkles include [Mouhou et al. 2021; Zuenko and Harders 2020]. Alternatively, the wrinkle patterns arising from base mesh deformation can be learned

from precomputed data. For a specific garment/character pair, Wang et al. [2010] precomputed a database containing the wrinkle patterns for different character poses, and applied them to a coarse simulation mesh at runtime. Neural techniques for this task have also been proposed recently [Zhang and Li 2024; Zhang et al. 2021], showing ability to generalize to novel garments beyond the ones in the training set. However, existing learned models do not account for the temporal dynamics of wrinkles, and as a result the synthesized results tend to exhibit fairly static wrinkles that fade in and out over time rather than sliding, merging, and splitting realistically. In addition, all previous techniques discussed in this paragraph treat only the wrinkle behaviour as driven by the base deformation, but do not consider the effect of wrinkles on the mechanical response of the base deformation itself. Consequently, they will be affected by locking artifacts when applied on coarse simulation meshes.

Along these lines, we also note several techniques for augmenting coarse models with wrinkles by performing additional simulation at high resolution, coupled with the coarse deformation Bergou et al. [2007]; Chen et al. [2023b]; Müller and Chentanez [2010]; Rémillard and Kry [2013]. However, these incur an additional computational expense for the high-resolution simulation.

Wrinkle mechanics has been extensively studied in physics. For instance, Cerdá and Mahadevan [2003] show the relationship between wrinkle wavelengths and amplitudes for a stretched thin sheet, assuming that wrinkles form only in the direction perpendicular to the base shell. Healey et al. [2013] give physical bounds for the shape of a thin sheet to form wrinkle patterns. They show that the Foppl-von Karman theory fails to provide stable bifurcation solution for shells with large mid-surface strain, and use a pure Green strain model to model larger non-linear strain response in the wrinkled regions. Aharoni et al. [2017] parameterize wrinkling of skin-like thin shells using sinusoids and derive the relationship between compressive strain, wrinkle wavelength and amplitudes. While these methods describe the overall relationship between material properties, sheet geometry, and wrinkling behavior, they cannot directly be applied to dynamic simulations where both the base mesh configuration and the wrinkle directions are varying over time.

Recently Chen et al. [2021] proposed tension-field wrinkles (TFW), a physics-based method for modeling wrinkle behaviour without requiring an additional fine-resolution mesh. Their model is based on the model of Aharoni et al. [2017], modeling a wrinkled sheet as a coarse base mesh, along with wrinkle correction terms parameterized by amplitude and spatial frequency. Inspired by the idea of reducing compression resistance to avoid locking in coarse base mesh [Jin et al. 2017], they model the base mesh's strain energy using tension field theory: in essence, the model resists stretching but allows unconditional compression. Unfortunately, their model lacks coupling between wrinkling and coarse mesh deformation. For instance, a highly wrinkled region might cause the base mesh to move due to higher compression in the region and collision between the triangles of the same cloth, but their model lacks this coupling. Another limitation of their work is that it only computes static drapes, and does not support animation.

3 Dynamic wrinkling

We extend Chen et al. [2021]'s work on parametric wrinkling and propose a framework for dynamic cloth simulations that capture wrinkling over coarse meshes. We use same fundamental wrinkle parameterization over coarse mesh model, however, the discrete representation varies from their model. The section is divided into three parts, first we see the continuum model and the discretization used for cloth deformation, next we explain the dynamic equations and constraints. Finally, we explain the wrinkle field reconstruction step.

148 3.1 Preliminaries

149 We represent cloth mesh as elastic thin shell of fixed thickness h . Kirchoff Love assumption allows
 150 us to represent deformation in the thin shell as a function of it's mid-surface $\mathbf{r}(u, v) : \Omega \rightarrow \mathbb{R}^3$ and
 151 normal displacement along the thickness. Instead of representing the cloth mesh exactly as the
 152 thin shell, we assume wrinkled thin-shell that assumes parametric sinusoids to model wrinkling
 153 over the shell mid-surface [Chen et al. 2021].

$$154 \quad 155 \quad \mathbf{r}(u, v) = \mathbf{r}_b(u, v) + d\mathbf{r}_b(u, v)\mathbf{v}_t(u, v) + a \cos \Phi \hat{\mathbf{n}}(u, v) \quad (1)$$

156 here $\mathbf{r}_b(u, v)$ is the mid-surface and $\hat{\mathbf{n}}(u, v)$ is the normal vector. The sinusoidal wave is param-
 157 eterized by the wrinkle parameters amplitude (a) and frequency Φ . The term $d\mathbf{r}_b(u, v)\mathbf{v}_t(u, v) =$
 158 $d\mathbf{r}_b(v_1 \sin \Phi + v_2 \sin 2\Phi)$ adds in-plane wrinkle correction term and normal deformation $a \cos \Phi$.
 159 See Chen et al. [2021] for more details on the choice of wrinkle parameters and their significance.

160 The continuum sheet in equation 1 is discretized as coarse triangulated base mesh \mathbf{r}_b with
 161 wrinkle parameters a, Φ stored at the mesh vertices. We use St. Venant-Kirchoff elasticity model
 162 for wrinkled thin-shell, defined in terms of the differential first fundamental form \mathbf{I} , and second
 163 fundamental form \mathbf{II} respectively. The elastic energy of the deformed shell is given by:

$$164 \quad 165 \quad U = \frac{1}{2} \int_{\Omega} \left(\frac{h}{4} E_s + \frac{h^3}{12} E_b \right) \sqrt{\det(\bar{\mathbf{I}})} dudv, E_s = \|\bar{\mathbf{I}}^{-1}(\mathbf{I} - \bar{\mathbf{I}})\|_{SV}^2, E_b = \|\bar{\mathbf{II}}^{-1}(\mathbf{II} - \bar{\mathbf{II}})\|_{SV}^2 \quad (2)$$

166 here, $\bar{\mathbf{I}}$ and $\bar{\mathbf{II}}$ represent rest fundamental forms respectively. See Chen et al. [2018] for the derivations
 167 and relation to the deformation-gradient based definition. The norm $\|\cdot\|_{SV}$ is a function of material
 168 Lamè parameters α and β : $\|\cdot\|_{SV}^2 = \frac{\alpha}{2} \text{tr}^2(\cdot) + \beta \text{tr}(\cdot)^2$. This shell energy can be extended to wrinkled
 169 shell by deriving the differential forms in terms of the wrinkled shell $\mathbf{I} = d\mathbf{r}^T d\mathbf{r}$, and $\mathbf{II} = d\mathbf{r}^T d\hat{\mathbf{n}}$. We
 170 can derive exact elastic energy for the mesh using these differential quantities, however, periodic
 171 wrinkle parameters add the scope for coarse-graining that simplify the wrinkled shell energy.
 172 Section 3.2 contains the wrinkled shell energy in terms of these differential forms.

173 3.2 Dynamic simulation of wrinkle mesh

174 We derive the dynamic equations of motion for the wrinkle shell using the Lagrangian formulation
 175 in terms of the generalized degrees of freedom (DoF) in our system. The degrees of freedom defining
 176 the deformations of the wrinkle shell \mathbf{r} are $\mathbf{q} = [\mathbf{a}, \Phi, \mathbf{r}_b]^t$, where \mathbf{a} and Φ comprise the sinusoidal
 177 high-frequency variations and \mathbf{r}_b captures the coarse mesh deformation. Moreover, we take the
 178 same assumptions on these DoFs based on their physical characteristics. The assumptions are:

- 179 • Variations in sinusoidal amplitudes $d\mathbf{a}$ are small at mesh triangle level,
- 180 • Phase Φ vary rapidly, capturing the high frequency variations, though their variation ($d\Phi$)
 remain constant at the triangle level,
- 181 • Positions \mathbf{r}_b capture low frequency deformations.

182 An important aspect to see here is that the last assumption fails for dense meshes as the position
 183 updates themselves would take care of the high frequency deformations rendering wrinkle
 184 parameters irrelevant. The results in section ?? show this behavior.

185 The lagrangian equations for generalized DoFs \mathbf{q} are given by:

$$186 \quad 187 \quad \frac{d}{dt} \left(\frac{\partial T}{\partial \dot{\mathbf{q}}} \right) + \frac{\partial U}{\partial \mathbf{q}} = 0 \quad (3)$$

188 here, $T = (1/2)\dot{\mathbf{q}}^T \mathbf{M} \dot{\mathbf{q}}$ is the kinetic energy of the particles in the system and $U : \mathbb{R}^N \rightarrow \mathbb{R}$ is the
 189 total potential energy, $\dot{\mathbf{q}}$ represents the time derivative of $\mathbf{q} \in \mathbb{R}^N$, $\mathbf{M}^{N \times N}$ is the mass matrix, where
 190 $N = \# \text{vertices} \times 5$ is the number of DoFs in the system.

Now, we derive the dynamics equations for the wrinkle shell (eq. 1). We ignore the in-plane correction term v_t as it does not effect the motion of mesh over time since the motion is dominated by the coarse base mesh \mathbf{r}_b deformation and the normal correction term $\hat{\mathbf{n}}$. We use $\mathbf{r} \approx \mathbf{r}_b + a \cos \Phi \hat{\mathbf{n}}_b$. T can be derived as follows:

$$\begin{aligned} \frac{1}{2} \dot{\mathbf{r}}^T \mathbf{M} \dot{\mathbf{r}} &= \frac{1}{2} (\dot{\mathbf{r}}_b^T \mathbf{M} \dot{\mathbf{r}}_b) + \frac{1}{2} (\dot{\mathbf{r}}_b^T \mathbf{M} \hat{\mathbf{n}}_b) [2\dot{a} \cos \Phi - 2a \sin \Phi \dot{\Phi}] + \frac{1}{2} (\dot{\mathbf{r}}_b^T \mathbf{M} \hat{\mathbf{n}}_b) [2a \cos \Phi] \\ &\quad + \frac{1}{2} (\hat{\mathbf{n}}_b^T \mathbf{M} \dot{\mathbf{r}}_b) [2\dot{a}a \cos^2 \Phi - a^2 \sin 2\Phi \dot{\Phi}] + \frac{1}{2} (\hat{\mathbf{n}}_b^T \mathbf{M} \dot{\mathbf{r}}_b) [a^2 \cos^2 \Phi] \\ &\quad + \frac{1}{2} (\hat{\mathbf{n}}_b^T \mathbf{M} \hat{\mathbf{n}}_b) [\dot{a}^2 \cos^2 \Phi + a^2 \sin^2 \Phi \dot{\Phi}^2 - a\dot{a} \sin 2\Phi \dot{\Phi}] \end{aligned} \quad (4)$$

The coarse grained kinetic energy $T^{cg} = (1/2)\dot{\mathbf{r}}^T \mathbf{M} \dot{\mathbf{r}}^{(cg)}$ is given by:

$$T^{(cg)} = \frac{1}{2} \left(\dot{\mathbf{r}}_b^T \mathbf{M} \dot{\mathbf{r}}_b + \frac{a^2}{2} \dot{\hat{\mathbf{n}}}^T_b \mathbf{M} \dot{\hat{\mathbf{n}}}_b + \frac{\dot{a}^2}{2} \hat{\mathbf{n}}^T_b \mathbf{M} \hat{\mathbf{n}}_b + \frac{a^2}{2} \dot{\Phi}^2 \hat{\mathbf{n}}^T_b \mathbf{M} \hat{\mathbf{n}}_b \right) \quad (5)$$

We use the results from Chen et al. [2021] for deriving the potential energy T stored by the wrinkle shell (eq. 1) for a given deformation state \mathbf{q} . Moreover, as U is dependent on the spatial derivative of phase instead of the phase itself, we treat wrinkle frequency ($d\Phi$) as a DoF instead of wrinkle phase (Φ) in our formulation. Using equations 3 and 5, the dynamics equations of motions defining the motion of wrinkle shell are given by:

$$\mathbf{M} \begin{pmatrix} \ddot{\mathbf{r}}_b \\ 0.5\ddot{a} \end{pmatrix} = - \begin{pmatrix} \frac{\partial U}{\partial \mathbf{r}_b} \\ \frac{\partial U}{\partial a} \end{pmatrix}, d\Phi^* = \arg \min_{d\Phi} \tilde{U}(d\Phi) \quad (6)$$

We treat Φ as purely spatial quantity and ignore it's time derivative in the Lagrangian derivation. The energy $\tilde{U}(d\Phi) = U(a, d\Phi, \mathbf{r}_b)$ with a, \mathbf{r}_b fixed. This is one of our algorithm's limitation that needs future work.

3.3 Discretization and solver

We use finite triangle discretization for the base mesh \mathbf{r}_b with wrinkle parameters a, Φ stored per vertex. Since, we deal with wrinkle frequency $d\Phi$ instead of actual phase values, we ignore Φ during the dynamic simulation and use wrinkle frequencies ($d\Phi$) as vectors stored per face as one of the DoFs. Here we deviate from the discretization of Chen et al. [2021] where they stored spatial phase derivatives as edge one-forms. We benefit from the physically valid assumption that $d\Phi$ varies slowly over \mathbf{r}_b , thus, can be assumed to be constant for a face. Moreover, it allows us to use parallel local-solve instead of one big global solve for $d\Phi$ s over the entire mesh resulting in huge computational speedups.

Constraints on wrinkle parameters: U is prone to triangle inversion due to the non-convexity of StVK energy in compression regime. This is enhanced by the parametric wrinkle energy that allows wrinkle parameters to grow indefinitely causing inversion. The issue can be avoided by using the physical limit on compression of thin shells to restrict wrinkling. The constraint can be imposed per element of the mesh: for any triangle in the mesh, very high-frequency wrinkles will prevent further compression in the direction \mathbf{v} if $|\nabla \Phi \cdot \mathbf{v}| \leq (h/\pi) \|\mathbf{F}\mathbf{v}\|_2$. $\nabla \Phi$ is the wrinkle frequency and \mathbf{F} is the deformation gradient of the corresponding triangle. The above constraint is ensured by ensuring that the matrix $\mathbf{I} - (h/\pi)^2 \nabla \Phi \nabla \Phi^T$ is positive semi-definite. Another observation is that U is an even function in terms of a , thus, we can safely constrain amplitudes to be non-negative.

Incremental potential formulation: Algorithm 1 shows the simulation pipeline. We use the incremental potential formulation of the dynamics equation (6) that corresponds to finding states that minimize the incremental potential energy

ALGORITHM 1: SimulationStep

```

Input : [ $a^n, r_b^n, d\Phi^n, \Phi^n$ ], [ $\dot{a}^n, \dot{r}_b^n, \Phi^n$ ],  $\Delta t$ 
Output: [ $a^{n+1}, r_b^{n+1}, d\Phi^{n+1}, \Phi^{n+1}, r^{n+1}$ ]

 $a^{n+1} \leftarrow \text{VBD}(a^n, \Delta t);$ 
 $r_b^{n+1} \leftarrow \text{VBD}(r_b^n, \Delta t);$ 
 $d\Phi \leftarrow \text{InitWrinkleParams}(a^{n+1}, r_b^{n+1});$ 
 $d\Phi^{n+1} \leftarrow \arg \min_{d\Phi^*} \tilde{U}(d\Phi^*);$ 
 $\Phi^{n+1} \leftarrow \text{WrinkleFieldReconstruction}(d\Phi^{n+1}, \Phi^n);$ 
 $r^{n+1} \leftarrow \text{WrinkleUpsampling}(a^{n+1}, \Phi^{n+1}, r_b^{n+1})$ 

```

ALGORITHM 2: Vertex-Block-Descent

```

Input : [qn, ̇qn], Δt
Output: [qn+1, ̇qn+1]

̇q ← qn + Δtqn + Δt2qn; // Inertial Prediction
q ← ̇q for k = 1 to Niter do
    for c = 1 to Ncolors do
        for i ∈ Cc in parallel do
            gi ← ∇iE(q);
            Hii ← ∇ii2E(q);
            qi ← qi - Hii-1gi ; // Block Newton
        end
    end
end

```

$$\mathbf{E} = \frac{1}{2\Delta t^2} \|\mathbf{q} - \mathbf{q}^n\|_M^2 + U(\mathbf{q}). \quad (7)$$

We use an energy based formulation that penalizes $\|d\Phi\|$ if $\|d\Phi\| \times \text{average rest edge length} < \pi/2$. We add this penalty energy $C(d\Phi) = (\|d\Phi\| \times \text{average rest edge length} - \pi/2)^2$ to the incremental potential formulation to ensure that only high frequency variations are captured by wrinkle parameters.

We follow the parallel Vertex-Block-Descent style (VBD) for updating amplitudes and positions over time. Then, we initialize dΦs according to the principle axes of strain tensor and then optimize \tilde{U} for dΦ (eq. 6). An important factor to consider while using parallelized VBD steps is the number of iterations used for simulation. For our simulations, we observed that we need 5-20 iterations for position updates and 20 iterations for amplitude updates. See [Chen et al. \[2024\]](#) for more details on vertex-block-descent.

Final wrinkled mesh can be obtained by reconstructing wrinkle phase Φ from frequencies followed by reconstruction of the wrinkled mesh. Further details on phase reconstruction and up-sampling are provided in next section.

3.4 Wrinkle phase reconstruction

Advancing state vectors in eq. 6 provide updated amplitudes, positions and dΦs for the next state. Then, we recover Φs per vertex to obtain the final deformed state (1). Obtaining a valid set of compatible phase values at each frame and ensuring that the deformations are temporally coherent

over time is a challenging problem. This section contains the details on finding compatible and time-coherent phase field from frequency field.

Non-oriented wrinkles: Wrinkle frequencies are stored as vector quantities $d\Phi$ defined over the tangent space of each mesh triangle (Sec. 3.2). However, wrinkling is a non-orientable phenomenon and cannot be represented using oriented vector quantities. For example, wrinkling represented by a tangent vector $d\Phi$ can equivalently be represented by its negation $-d\Phi$; both of these states have the same wrinkle shell energy (2). Thus, orientation of wrinkling does not matter for defining the potential energy of the wrinkled shell. In other words, the wrinkle frequency distribution should be treated as a line field rather than a vector field. However, an oriented direction of $d\Phi$ is necessary for reconstructing phase values. In the following, we describe how we overcome this ambiguity.

Integrability: Integrability is not guaranteed as we do not enforce integrability constraint while solving for $d\Phi$ s in the static update step, and $d\Phi$ s obtained in the simulation update are almost never integrable. In essence, Φ is recoverable from a tangent vector field $d\Phi$, if and only if $\nabla \times d\Phi = 0$ that is not guaranteed in 6. Thus, we follow Chen et al. [2023a]’s idea of finding an approximate phase field that is compatible with $d\Phi$ s in a least-squares style optimization problem. To this end, we represent Φ field with a unit complex field $\psi \in \mathcal{M} : \Omega \rightarrow \mathbb{C}, |\psi| = 1, \arg \psi = \Phi$. Treating phase field as complex field is easier in optimization problems than with real numbers as it removes the periodic discontinuities, allowing us to use gradient based optimization methods. We optimize the following energy for Φ and ω consistency:

$$\psi = \arg \min_{\psi} \|(\mathbf{d} - i\omega)\psi\| \quad (8)$$

$$\|\psi\|=1, \omega=d\Phi \cdot \mathbf{v}, \forall \mathbf{v} \in T_x \Omega$$

Discretization and solver: $\psi \in \mathcal{M}$ is stored at mesh vertices. We solve 8 by computing the phase differences ω along edges from wrinkle frequencies $d\Phi$ on faces. For each edge between vertices i and j , we wish to compute the desired phase difference as $\omega = d\Phi \cdot e_{ij}$, with $d\Phi$ averaged from the adjacent edges. However, since $d\Phi$ contains a sign ambiguity, we perform non-oriented averaging by treating adjacent $d\Phi$ ’s as unit complex numbers, averaging their squares, and taking the square root. This allows us to avoid choosing an orientation for the face $d\Phi$ ’s, and hence for ω , which in any case cannot be done locally. In the phase reconstruction energy as well, we consider both signs $\pm\omega$ and take their averaged energy, as discussed below. We find that this is sufficient to align the gradient of the reconstructed phase with the target directions, without introducing any nondifferentiability into the objective function.

Reconstruction of phases at vertices: The task is now to find a distribution of ϕ that best agrees with ω obtained for each vertex. Instead of directly optimizing the phase reconstruction energy, we incorporate some dynamics into the phases as well, which enables a temporally coherent evolution of the phase distribution. Specifically, we include both a physics-inspired potential energy estimating the contribution of phase reconstruction error to the elastic energy, and an inertia term modeling the kinetic energy associated with phase changes.

The potential energy is determined by how much the computed phase aligns with those of adjacent vertices subject to the desired phase offsets. For each vertex i , its potential energy is

$$PE_i = \sum_{j \in N(i)} \lambda_{ij} \|\psi_i e^{i\omega_{ij}} - \psi_j\|^2 \quad (9)$$

where:

$$\lambda_{ij} = \beta \times \frac{h \times A_{ij} \times (\frac{a_i + a_j}{2})^2}{16|\mathbf{e}_{ij}|^2} \quad (10)$$

$$\mathcal{N}(i) := \{ j \mid \{i, j\} \in \text{Edges} \} \quad (11)$$

Here, A_{ij} represents an approximation of the area attributed to the edge $\{i, j\}$, obtained as $\frac{1}{3}$ times the sum of the adjacent face areas.

We also define a kinetic energy,

$$KE_i = \frac{1}{2} \frac{M_i a_i^2}{\Delta t^2} \|\psi_i^t - \psi_i^{t-1}\| \quad (12)$$

The total energy becomes,

$$E = \sum_{i \in \text{Vertices}} PE_i + KE_i \quad (13)$$

We get an exact minimizer for this energy:

$$\psi_i = \frac{H_i}{\|H_i\|} \quad (14)$$

$$H_i = \sum_{j \in \mathcal{N}(i)} (\lambda_{ij} \psi_j e^{-\iota \omega_{ij}}) + \frac{1}{2} \frac{M_i a_i^2}{\Delta t^2} \psi_i^{t-1} \quad (15)$$

To optimize this energy globally and across all vertices, we again utilize VBD.

Note that we obtain a non-oriented $\nabla \Phi$ per face from the solver, hence we need to define ω_{ij} across an edge. To solve this, we take four different values for ω_{ij} (two in the case of a boundary edge) for an edge $\{i, j\}$, given by

$$\nabla \Phi_{hij} \cdot \mathbf{e}_{ij}, \quad -\nabla \Phi_{hij} \cdot \mathbf{e}_{ij}, \quad \nabla \Phi_{ijk} \cdot \mathbf{e}_{ij}, \quad -\nabla \Phi_{ijk} \cdot \mathbf{e}_{ij}.$$

The energy for a vertex is then set as the average of the four distinct energies obtained from these values of ω .

Upsampling of mesh: We use the same upsampling and wrinkle application scheme defined in Chen et al. [2023a]’s work. With consistent gradients defined over vertices, we now calculate gradients over edges by again utilizing the line-field addition, further allowing us to calculate ω over each edge $\{i, j\}$ as $\nabla \Phi_{ij} \cdot \mathbf{e}_{ij}$. This is passed in as input to Chen et al. [2023a]’s scheme. The final deformed mesh at timestep then can be found by 1.

4 Results

We show the results in this section. All experiments are run on a machine with a 13th Gen Intel(R) Core(TM) i7-13700 CPU and 32 GB RAM, Ubuntu 24.04 operating system. The results showcase the efficacy of our parametric wrinkling framework for dynamic simulation of cloth. We use spatial hashing for broad-phase collision detection Teschner et al. [2003] and constrained particles sampled in the mesh for narrow-phase collision handling [Macklin et al. 2014]. All results reported here were generated using the VBD time integrator.

Draping behavior. Figure 2 shows the draping behavior of cloth on a sphere. A 1m × 1m discretized using just 256 vertices is allowed to fall under the influence of gravity on a sphere of radius 0.6m. High-frequency wrinkles are visible in the regions where the base mesh is compressed, and no wrinkling is visible in the top regions where the mesh is completely flat. The draping behavior, although not entirely physically accurate, still adds visual plausibility to the simulation. Similar results are obtained for cloth drape over Stanford bunny example in Fig. 3. We compare the visual quality of our results in this experiment, where we ran a reference simulation using a high-resolution cloth mesh with 4096 vertices. All material parameters remain the same. We use Chen et al. [2018]’s thin shell elastic model as the fabric model. Some visible differences remain between our results

ALGORITHM 3: Vertex-Block-Descent for Phase Reconstruction

Input : Face gradients $\nabla\Phi_f$, previous phases ψ^{t-1}, ψ^{t-2} , vertex masses M_x , wrinkle amplitudes a_x , edge lengths $|e_{xy}|$, edge areas Ar_{xy} , time step Δt

Output : Updated vertex phases ψ^t

397 Initialize $\psi \leftarrow \psi^{t-1}$;

398 **for** $k = 1$ **to** N_{outer} **do**

399 **for** $c = 1$ **to** N_{colors} **do**

400 **for** $x \in C_c$ **in parallel do**

401 $H_x \leftarrow 0$; // Initialize target accumulator

402 **for each face** f **incident on** x **do**

403 Derive edge-aligned phase offsets $\omega_{xy}^{(f)}$ from $\nabla\Phi_f$;

404 **for each valid sign choice** $\pm\omega_{xy}^{(f)}$ **do**

405 **for each neighbor** y **of** x **in** f **do**

406 $H_x \leftarrow H_x + \lambda_{xy}\psi_y e^{-i\omega_{xy}}$;

407 **end**

408 **end**

409 **end**

410 $H_x \leftarrow H_x + \frac{1}{2} \frac{M_x a_x^2}{\Delta t^2} \psi_x^{t-1} e^{i(1-k_d)(\phi_x^{t-1} - \phi_x^{t-2})}$; // Kinetic term

411 **if** $\|H_x\| > \varepsilon$ **then**

412 $\psi_x \leftarrow \frac{H_x}{\|H_x\|}$; // Exact minimizer

413 **end**

414 **end**

415 **end**

416 **if** $\|\psi - \psi_{prev}\| < \tau$ **then**

417 **break**; // Convergence

418 **end**

419 **end**

421

422

423

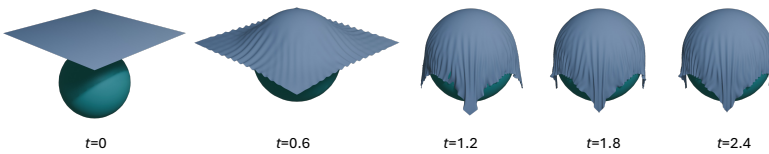


Fig. 2. Cloth drape over sphere. All timings are in seconds.

432 and the reference simulation. These differences can be attributed to the limitations of the base
433 mesh discretization itself. For example, the region between the bunny's ears exhibits completely
434 different cloth behavior, as large triangles in a coarse mesh cannot bend in those regions, whereas
435 smaller triangles can bend in those regions easily. However, when we compare the results at the
436 same mesh resolution as ours, our results are clearly better (see Fig. 4).

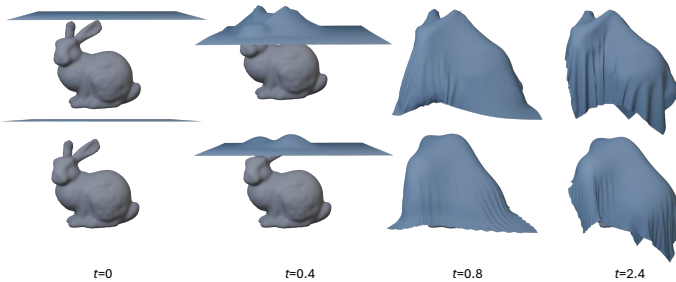
437
438 *Mesh dependence.* Fig. 5 shows cloth draping behavior when two edges of the cloth are fixed, and
439 the cloth is allowed to fall under gravity. Compression along the square cloth's diagonal introduces
440 wrinkling in the mesh in a direction orthogonal to compression. We compare our results with a

442 ALGORITHM 4: Line-Field-Based Reconstruction of Consistent Edge Omegas

443 **Input** : Per-face unoriented gradients $\{\nabla\Phi_f\}$, vertex positions \mathbf{V} , mesh connectivity (V, F, E)
 444 **Output**: Consistent edge phase offsets $\{\omega_{ij}\}$
 445
Vertex Line-Field Aggregation:
 446 **for** each vertex x **do**
 447 Collect gradients $\{g_f\}$ from all incident faces $f \ni x$;
 448 Compute a sign-invariant average using line-field addition;
 449 Store the resulting vertex gradient $\nabla\phi_x$;
 450 **end**
 451
Edge Line-Field Aggregation and Projection:
 452 **for** each edge $\{i, j\} \in E$ **do**
 453 Retrieve vertex gradients $\nabla\phi_i$ and $\nabla\phi_j$;
 454 Compute a line-field average to obtain a consistent edge direction $\bar{\nabla}\phi_{ij}$;
 455 Compute the edge phase offset:
 456 $\omega_{ij} \leftarrow \bar{\nabla}\phi_{ij} \cdot \mathbf{e}_{ij}$
 457 **end**
 458
return $\{\omega_{ij}\}$;
 459
 460

461 Table 1. Material parameters for our simulations. Y: Young's Modulus, v: Poisson's Ratio, h: thickness, dt:
 462 timestep, ρ : density
 463

464	Model	Material Properties				
		Y	v	h(m)	dt(s)	ρ
467	Cylinder twist	500000	0.25	0.0001	0.01	0.276
468	Cloth drape under gravity	10000	0.5	0.001	0.01	0.05
469	Cloth drape over sphere	20000	0.3	0.001	0.005	0.1
470	Cloth drape over bunny	50000	0.3	0.0005	0.005	0.224
471	Sleeve wrinkling	12000	0.1	0.005	0.01	0.276



483 Fig. 3. Cloth drape over bunny. The top row shows high-resolution reference simulation results (4096 vertices),
 484 and the bottom row shows our result (256 vertices). Our method provides similar results to a high-resolution
 485 reference in compression-dominated regions.
 486

488 high-resolution reference simulation (4096 vertices), and we observe that our method can capture
 489 the very high-frequency wrinkling on very coarse meshes (64 vertices). This provides a significant
 490



Fig. 4. Cloth drape over bunny. Left: Low resolution cloth used for simulation (256 vertices), Center: our result, Right: high resolution reference simulation results (4096 vertices). Elastic shell simulation with the same level of coarseness as ours is unable to generate a visually plausible cloth drape.

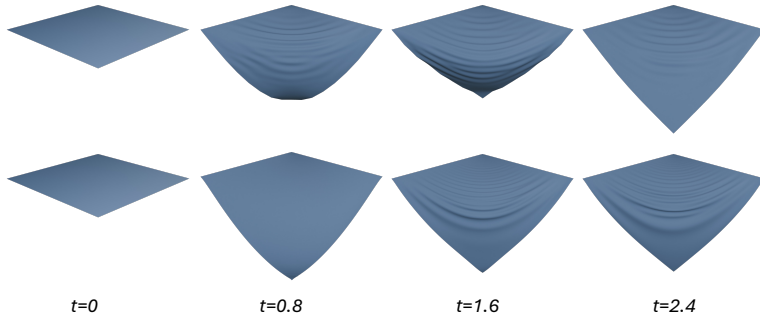


Fig. 5. Cloth drape under gravity with two edges fixed. Our result is shown in the top row, and the high-resolution reference simulation is shown in the bottom row.

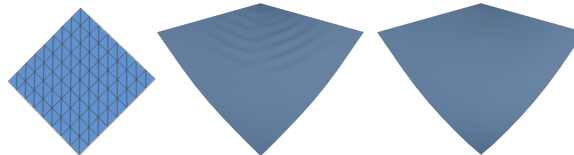


Fig. 6. Left: Mesh discretization, the top two edges are clamped. The mesh discretization does not allow bending along the mesh diagonal, resulting in locking artifacts visible in the coarse simulation shown on the Right. Center: simulation obtained using the same discretization shows visually plausible wrinkling in cloth.

computational speedup compared to a high-resolution simulation, making our simulation more interactive. Timings provided in table 2 and table 3 show that our method is 136x faster than a high-resolution simulation. Another interesting phenomenon observed with our method is the reduction of locking artifacts. In the Figure. In 6, we can observe that when the mesh discretization is such that the bending direction does not align with it, locking is observed in coarse simulations. In contrast, our results show high-frequency wrinkling, similar to that obtained in discretizations where bending is allowed, and no locking occurs.

Twisting experiments. We perform a cylinder twist experiment to visualize the dynamic wrinkle appearance in a scene where one end of the cylinder is rotated in clockwise direction. It is a good

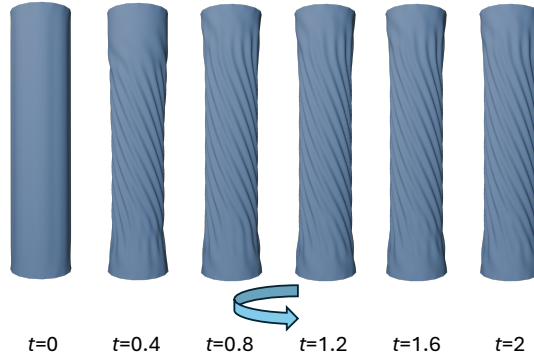


Fig. 7. Cloth is put on a cylinder with its top vertices fixed. The bottom vertices are rotated gradually. Wrinkling can be observed on the cylinder surface over time, from the bottom end to the top.



Fig. 8. Wrinkling observed in the sleeve at the joint between two cylinders.

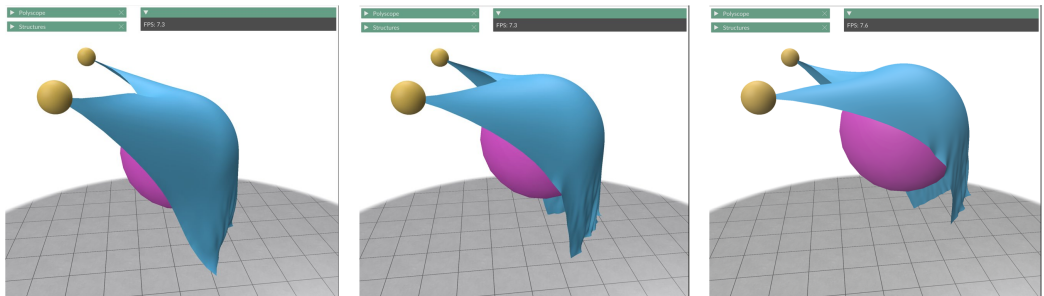


Fig. 9. We can observe that our wrinkling model runs at 7-8fps, hence achieving interactive rates.

example for testing high-frequency wrinkling, where an increase in twisting introduces wrinkles in the mesh from one end to the other. Simulation frame at time $t = 0$ s shows flat configuration Fig. 7. Vertices in the bottom ring of the cylinder are rotated in clockwise direction, keeping the vertices of the top ring fixed. The example shows wrinkle propagation from bottom to top as the cylinder is twisted. Our results show high-frequency wrinkles that keep getting consistent over time.

Real world cloth. We set up a cloth sleeve example that mimics the wrinkling observed in the cloth sleeve over the arm at the elbow joint as the arms bend. The scene is set up with two cylinders joined via a ball in the middle. Visually plausible buckling patterns can be seen in the simulation when the joint is bent (Fig. 8).

Tables 2 and 3 show timing statistics of our method and a high-resolution cloth simulation. We report the average time required per simulation frame for performing the dynamic solve for base mesh and wrinkle parameters, phase reconstruction, and upsampling. It is evident that our

Table 2. Average simulation time per time step data for our dynamic wrinkle simulation.

Model	#Vertices	Average time per simulation frame		
		Dynamic solve (ms)	Phase reconstruction (ms)	Loop upsampling (ms)
Cylinder twist	256		0.570	79.944
Cloth drape under gravity	64	10	0.223	22.358
Cloth drape over sphere	256	20	0.468	79.868
Cloth drape over bunny	256	50	0.541	86.580
Sleeve wrinkling	256	50	0.729	85.617

Table 3. Average simulation time per frame for high resolution simulations. Note that we are using StVK energy 2 instead of our wrinkled shell for these simulations.

Model	#Vertices	Dynamic solve (s)
Cloth drape under gravity	4096	1.36
Cloth drape under gravity	64	0.0049
Cloth drape over bunny	4096	4.4
Cloth drape over sphere	256	0.01

dynamic solve and phase reconstruction steps have significantly shorter computation times than the average frame generation time in a high-resolution mesh simulation, and our method can be used in interactive simulations. However, Loop upsampling is the bottleneck in the simulation that needs future work.

5 Conclusion

We show that dynamic wrinkling is a feasible approach for detailed, physically consistent cloth animation on coarse meshes at interactive rates. Building on the wrinkle parameterization introduced by [Chen et al. 2021], we have introduced a dynamics model for a cloth sheet represented as a superposition of a base surface and a wrinkle distribution parameterized by spatially varying amplitude and frequency. Derived from Lagrangian mechanics by coarse-graining over wrinkle periods, our model naturally incorporates two-way coupling of the base surface and the wrinkle parameters, allowing the base deformation to drive emergence of wrinkles and permitting compression of the base surface in turn. To actually deform the mesh using the computed wrinkle parameters, we also introduce a simple phase reconstruction strategy that, combined with wrinkle upsampling [Chen et al. 2023b], produces dynamically evolving, temporally coherent wrinkles on the simulated mesh.

5.1 Discussion and limitations

A unique feature of our approach is that the elastic response of the base mesh is coupled with the wrinkle parameters. While existing approaches such as inequality cloth [Jin et al. 2017] and tension field wrinkles [Chen et al. 2021] unconditionally remove all compression resistance from the elasticity model, in our model the compression resistance of the material decreases naturally with the emergence of wrinkles. This opens the door to allowing more realistic material models to be used, for example those estimated from observations [Clyde et al. 2017; Miguel et al. 2012; Zhang et al. 2025] or computed by homogenization [Sperl et al. 2020]. It is unclear how to incorporate these in previous models, but our coarse-graining methodology can support these in principle. This

is a promising avenue for future work, which would enable detailed simulation of more realistic fabric models in real time.

We were hopeful that the reduced compression resistance arising from wrinkle formation would eliminate locking artifacts in coarse simulations, but this did not turn out to be the case. For example, a square cloth mesh with all diagonals aligned in one direction exhibits artificial resistance to bending in the perpendicular direction. We found that this issue arises because non-aligned bending produces not just compression (along triangle edges) but also tension (along face altitudes). The TFW model [Chen et al. 2021] suffers from the same locking problem, while inequality cloth [Jin et al. 2017] which uses only edge springs does not. To obtain coarse simulation results that are more consistent with the ground truth, this is an important problem that deserves further study.

There are several other potential extensions to the proposed technique that we hope to pursue in future work. First, since the wrinkle amplitudes are tracked as part of the base mesh simulation, it would be possible to incorporate them in the collision processing step as well, effectively treating the sheet as “thickened” by the wrinkle amplitude. This could even allow two-way coupling between wrinkles and contact, so that larger amplitudes could push the mid-surface away from obstacles, while regions in tight contact would be forced to have smaller amplitudes and higher frequencies. Secondly, we only have a rudimentary modeling of phase dynamics at present. It would be interesting to have a more sophisticated model including influences from external forces, so that for example the wrinkles in a flag could be pushed along by the wind.

Finally, we inherit from Chen et al. [2021] the limitation that wrinkles are assumed to have locally a single frequency and direction: the wrinkle parameterization does not allow for superposition of multiple intersecting wrinkles, or more complex buckling patterns such as the diamond buckling seen in compressed, curved sheets. It may be possible to extend the model to allow for a superposition of multiple amplitude/frequency fields. More generally, an exciting possibility is to switch from the manually designed wrinkle parameterization to a learned representation that can span the range of local wrinkling and buckling patterns. Such a combination of coarse simulation and learned fine-scale details has been explored in previous works, but they do not achieve dynamic wrinkle behaviour and do not incorporate sheet mechanics in the learned models. We are excited to explore this direction in future work.

667

668 References

- 669 Hillel Aharoni, Desislava V. Todorova, Octavio Albarrán, Lucas Goehring, Randall D. Kamien, and Eleni Katifori. 2017. The
670 smectic order of wrinkles. *Nature Communications* 8, 1 (18 Jul 2017), 15809. [doi:10.1038/ncomms15809](https://doi.org/10.1038/ncomms15809)
- 671 Miklós Bergou, Saurabh Mathur, Max Wardetzky, and Eitan Grinspun. 2007. TRACKS: toward directable thin shells. *ACM
672 Trans. Graph.* 26, 3 (July 2007), 50–es. [doi:10.1145/1276377.1276439](https://doi.org/10.1145/1276377.1276439)
- 673 David Edward Breen. 1993. *A particle-based model for simulating the draping behavior of woven cloth*. Ph.D. Dissertation.
USA. UMI Order No. GAX94-05658.
- 674 E. Cerdá and L. Mahadevan. 2003. Geometry and Physics of Wrinkling. *Phys. Rev. Lett.* 90 (Feb 2003), 074302. Issue 7.
[doi:10.1103/PhysRevLett.90.074302](https://doi.org/10.1103/PhysRevLett.90.074302)
- 675 Anka He Chen, Ziheng Liu, Yang Yin, and Cem Yuksel. 2024. Vertex Block Descent. *ACM Transactions on Graphics (TOG)*
116 (2024).
- 677 Hsiao-Yu Chen, Arnav Sastry, Wim M. van Rees, and Etienne Vouga. 2018. Physical simulation of environmentally induced
678 thin shell deformation. *ACM Trans. Graph.* 37, 4, Article 146 (jul 2018), 13 pages. [doi:10.1145/3197517.3201395](https://doi.org/10.1145/3197517.3201395)
- 679 Yunuo Chen, Tianyi Xie, Cem Yuksel, Danny Kaufman, Yin Yang, Chenfanfu Jiang, and Minchen Li. 2023b. Multi-layer Thick
680 Shells. *ACM Transactions on Graphics (Proceedings of SIGGRAPH 2023)* 42, 4 (07 2023), 14 pages. [doi:10.1145/3592143](https://doi.org/10.1145/3592143)
- 681 Zhen Chen, Hsiao-Yu Chen, Danny M. Kaufman, Mélina Skouras, and Etienne Vouga. 2021. Fine Wrinkling on Coarsely
682 Meshed Thin Shells. *ACM Trans. Graph.* (8 2021).
- 683 Zhen Chen, Danny Kaufman, Mélina Skouras, and Etienne Vouga. 2023a. Complex Wrinkle Field Evolution. *ACM Trans.
684 Graph.* 42, 4, Article 72 (jul 2023), 19 pages. [doi:10.1145/3592397](https://doi.org/10.1145/3592397)
- 685 Kwang-Jin Choi and Hyeong-Seok Ko. 2002. Stable but responsive cloth. In *Proceedings of the 29th Annual Conference
686 on Computer Graphics and Interactive Techniques* (San Antonio, Texas) (SIGGRAPH '02). Association for Computing

- 687 Machinery, New York, NY, USA, 604–611. doi:[10.1145/566570.566624](https://doi.org/10.1145/566570.566624)
- 688 Gabriel Cirio, Jorge Lopez-Moreno, David Miraut, and Miguel A. Otaduy. 2014. Yarn-level simulation of woven cloth. *ACM Trans. Graph.* 33, 6, Article 207 (Nov. 2014), 11 pages. doi:[10.1145/2661229.2661279](https://doi.org/10.1145/2661229.2661279)
- 689 David Clyde, Joseph Teran, and Rasmus Tamstorf. 2017. Modeling and data-driven parameter estimation for woven fabrics. In *Proceedings of the ACM SIGGRAPH / Eurographics Symposium on Computer Animation* (Los Angeles, California) (SCA '17). Association for Computing Machinery, New York, NY, USA, Article 17, 11 pages. doi:[10.1145/3099564.3099577](https://doi.org/10.1145/3099564.3099577)
- 690 Elliot English and Robert Bridson. 2008. Animating developable surfaces using nonconforming elements. In *ACM SIGGRAPH 2008 Papers* (Los Angeles, California) (SIGGRAPH '08). Association for Computing Machinery, New York, NY, USA, Article 66, 5 pages. doi:[10.1145/1399504.1360665](https://doi.org/10.1145/1399504.1360665)
- 691 Russell Gillette, Craig Peters, Nicholas Vining, Essex Edwards, and Alla Sheffer. 2015. Real-time dynamic wrinkling of coarse animated cloth. In *Proceedings of the 14th ACM SIGGRAPH / Eurographics Symposium on Computer Animation* (Los Angeles, California) (SCA '15). Association for Computing Machinery, New York, NY, USA, 17–26. doi:[10.1145/2786784.2786789](https://doi.org/10.1145/2786784.2786789)
- 692 Rony Goldenthal, David Harmon, Raanan Fattal, Michel Bercovier, and Eitan Grinspun. 2007. Efficient simulation of inextensible cloth. *ACM Trans. Graph.* 26, 3 (July 2007), 49–es. doi:[10.1145/1276377.1276438](https://doi.org/10.1145/1276377.1276438)
- 693 Timothy J. Healey, Qingdu Li, and Ron-Bin Cheng. 2013. Wrinkling Behavior of Highly Stretched Rectangular Elastic Films via Parametric Global Bifurcation. *Journal of Nonlinear Science* 23, 5 (01 Oct 2013), 777–805. doi:[10.1007/s00332-013-9168-3](https://doi.org/10.1007/s00332-013-9168-3)
- 694 Ning Jin, Wenlong Lu, Zhenglin Geng, and Ronald P. Fedkiw. 2017. Inequality cloth. In *Proceedings of the ACM SIGGRAPH / Eurographics Symposium on Computer Animation* (Los Angeles, California) (SCA '17). Association for Computing Machinery, New York, NY, USA, Article 16, 10 pages. doi:[10.1145/3099564.3099568](https://doi.org/10.1145/3099564.3099568)
- 695 Jonathan M. Kaldor, Doug L. James, and Steve Marschner. 2008. Simulating knitted cloth at the yarn level. *ACM Trans. Graph.* 27, 3 (Aug. 2008), 1–9. doi:[10.1145/1360612.1360664](https://doi.org/10.1145/1360612.1360664)
- 696 Woojong Koh, Rahul Narain, and James F. O'Brien. 2015. View-Dependent Adaptive Cloth Simulation with Buckling Compensation. *IEEE Transactions on Visualization and Computer Graphics* 21, 10 (2015), 1138–1145. doi:[10.1109/TVCG.2015.2446482](https://doi.org/10.1109/TVCG.2015.2446482)
- 697 Miles Macklin, Matthias Müller, Nuttapong Chentanez, and Tae-Yong Kim. 2014. Unified particle physics for real-time applications. *ACM Trans. Graph.* 33, 4 (2014), 153:1–153:12. doi:[10.1145/2601097.2601152](https://doi.org/10.1145/2601097.2601152)
- 698 E. Miguel, D. Bradley, B. Thomaszewski, B. Bickel, W. Matusik, M. A. Otaduy, and S. Marschner. 2012. Data-Driven Estimation of Cloth Simulation Models. *Computer Graphics Forum* 31, 2pt2 (2012), 519–528. arXiv:<https://onlinelibrary.wiley.com/doi/10.1111/j.1467-8659.2012.03031.x> doi:[10.1111/j.1467-8659.2012.03031.x](https://doi.org/10.1111/j.1467-8659.2012.03031.x)
- 699 A. Ait Mouhou, A. Saaidi, M. Ben Yakhlef, and K. Abbad. 2021. Wrinkle synthesis for cloth mesh with hermite radial basis functions. 80, 1 (Jan. 2021), 1583–1610. doi:[10.1007/s11042-020-09743-3](https://doi.org/10.1007/s11042-020-09743-3)
- 700 Matthias Müller and Nuttapong Chentanez. 2010. Wrinkle meshes. In *Proceedings of the 2010 ACM SIGGRAPH/Eurographics Symposium on Computer Animation* (Madrid, Spain) (SCA '10). Eurographics Association, Goslar, DEU, 85–92.
- 701 Rahul Narain, Armin Samii, and James F. O'Brien. 2012. Adaptive anisotropic remeshing for cloth simulation. *ACM Trans. Graph.* 31, 6, Article 152 (Nov. 2012), 10 pages. doi:[10.1145/2366145.2366171](https://doi.org/10.1145/2366145.2366171)
- 702 Xavier Provot. 2001. Deformation Constraints in a Mass-Spring Model to Describe Rigid Cloth Behavior. *Graphics Interface* 23(19) (09 2001).
- 703 Olivier Rémiillard and Paul G. Kry. 2013. Embedded thin shells for wrinkle simulation. *ACM Trans. Graph.* 32, 4, Article 50 (July 2013), 8 pages. doi:[10.1145/2461912.2462018](https://doi.org/10.1145/2461912.2462018)
- 704 Damien Rohmer, Stefanie Hahmann, and Marie-Paule Cani. 2010. Wrinkle synthesis for cloth mesh with Hermite radial basis functions. *Computer Graphics Forum* 29, 6 (2010), 1813–1824. doi:[10.1111/j.1467-8659.2010.01717.x](https://doi.org/10.1111/j.1467-8659.2010.01717.x)
- 705 Georg Sperl, Rahul Narain, and Chris Wojtan. 2020. Homogenized yarn-level cloth. *ACM Trans. Graph.* 39, 4, Article 48 (Aug. 2020), 16 pages. doi:[10.1145/3386569.3392412](https://doi.org/10.1145/3386569.3392412)
- 706 Matthias Teschner, Bruno Heidelberger, Matthias Müller, Danat Pomerantes, and Markus H. Gross. 2003. Optimized Spatial Hashing for Collision Detection of Deformable Objects. In *8th International Fall Workshop on Vision, Modeling, and Visualization, VMV 2003, München, Germany, November 19-21, 2003*. Thomas Ertl (Ed.). Aka GmbH, 47–54.
- 707 Bernhard Thomaszewski, Markus Wacker, and Wolfgang Straßer. 2006. A consistent bending model for cloth simulation with corotational subdivision finite elements. 107–116. doi:[10.1145/1218064.1218079](https://doi.org/10.1145/1218064.1218079)
- 708 Huamin Wang. 2021. GPU-based simulation of cloth wrinkles at submillimeter levels. *ACM Trans. Graph.* 40, 4, Article 169 (July 2021), 14 pages. doi:[10.1145/3450626.3459787](https://doi.org/10.1145/3450626.3459787)
- 709 Huamin Wang, Florian Hecht, Ravi Ramamoorthi, and James F. O'Brien. 2010. Example-based wrinkle synthesis for clothing animation. 29, 4, Article 107 (July 2010), 8 pages. doi:[10.1145/1778765.1778844](https://doi.org/10.1145/1778765.1778844)
- 710 Diyang Zhang, Zhendong Wang, Zegao Liu, Ximeng Pei, Weiwei Xu, and Huamin Wang. 2025. Physics-inspired Estimation of Optimal Cloth Mesh Resolution. In *Proceedings of the Special Interest Group on Computer Graphics and Interactive Techniques Conference Conference Papers (SIGGRAPH Conference Papers '25)*. Association for Computing Machinery, New York, NY, USA, Article 23, 11 pages. doi:[10.1145/3721238.3730619](https://doi.org/10.1145/3721238.3730619)

- 736 Meng Zhang and Jun Li. 2024. Neural Garment Dynamic Super-Resolution. In *SIGGRAPH Asia 2024 Conference Papers*
737 (Tokyo, Japan) (SA '24). Association for Computing Machinery, New York, NY, USA, Article 122, 11 pages. doi:10.1145/
738 3680528.3687610
- 739 Meng Zhang, Tuanfeng Wang, Duygu Ceylan, and Niloy J. Mitra. 2021. Deep Detail Enhancement for Any Garment.
740 *Computer Graphics Forum* 40, 2 (2021), 399–411. arXiv:<https://onlinelibrary.wiley.com/doi/pdf/10.1111/cgf.142642> doi:10.
741 1111/cgf.142642
- 742 Evgeny Zuenko and Matthias Harders. 2020. Wrinkles, Folds, Creases, Buckles: Small-Scale Surface Deformations as
743 Periodic Functions on 3D Meshes. *IEEE Transactions on Visualization and Computer Graphics* 26, 10 (2020), 3077–3088.
744 doi:10.1109/TVCG.2019.2914676
- 745
- 746
- 747
- 748
- 749
- 750
- 751
- 752
- 753
- 754
- 755
- 756
- 757
- 758
- 759
- 760
- 761
- 762
- 763
- 764
- 765
- 766
- 767
- 768
- 769
- 770
- 771
- 772
- 773
- 774
- 775
- 776
- 777
- 778
- 779
- 780
- 781
- 782
- 783
- 784